PCCP

Accepted Manuscript

ROYAL SOCIETY OF CHEMISTRY

www.rsc.org/pccp

Physical Chemistry Chemical Physics RSCPublishing

ARTICLE

In-situ strain evolution during a disconnection event in a battery nanoparticle

ite this: DOI: 10.1039/x0xx00000x

Andrew Ulvestad,[a] Jesse N. Clark,[b,c] Andrej Singer,[a] , David Vine,[d] H.M. Cho,[e] Ross Harder,[d] Ying Shirley Meng,[e] and Oleg G. Shpyrko[a]

Received 00th January 2012,
Accepted 00th January 2012

DOI: 10.1039/x0xx00000x

www.rsc.org/

Lithium ion batteries are the dominant form of energy storage in mobile devices, increasingly employed in transportation, and likely candidates for renewable energy storage and integration into the electrical grid. To fulfil their powerful potential, electrodes with increased capacity, faster charge rates, and longer cycle life must be developed. Understanding the mechanics and chemistry of individual nanoparticles under *in-situ* conditions is a crucial step to improving performance and mitigating damage. Here we reveal 3D strain evolution within a single nanoparticle of a promising high voltage cathode material, $LiNi_{0.5}Mn_{1.5}O_4$, under *in-situ* conditions. The particle becomes disconnected during the second charging cycle. This is attributed to the formation of a cathode electrolyte interphase layer with slow ionic conduction. The three-dimensional strain pattern within the particle is independent of cell voltage after disconnection, indicating that the particle is unable to redistribute lithium within its volume or to its neighbours. Understanding the disconnection process at the single particle level and the equilibrium or non-equilibrium state of nanoparticles is essential to improving performance of current and future electrochemical energy storage systems.

Introduction

Lithium-ion batteries can become the de facto choice for high power energy storage solutions in both transportation and the integrated smart power grid provided the degradation of electrochemical performance during use can be understood, mitigated, and ideally eliminated[1,2]. Spinel materials such as disordered $LiNi_{0.5}Mn_{1.5}O_4$ (LNMO) are appealing as high voltage, high capacity, environmentally friendly, and low cost cathodes for use in numerous markets[3]. However, capacity loss due to degradation is limiting its current use.

[a] *Department of Physics, University of California-San Diego, La Jolla, California 92093-0319*
[b] *Stanford PULSE Institute, SLAC National Accelerator Laboratory, Menlo Park, California 94025*
[c] *Center for Free-Electron Laser Science (CFEL), Deutsches Elektronensynchrotron (DESY) Notkestrasse 85, 22607 Hamburg, Germany*
[d] *Advanced Photon Source, Argonne National Laboratory, Argonne, Illinois 60439*
[e] *Department of NanoEngineering, University of California-San Diego, La Jolla, California 92093-0448*

Important degradation effects[4] include active material cracking[5], electrochemical disconnection, and impedance increase due to the formation of electrode electrolyte interphases[6]. Disconnection is an important process as it leads to loss of active material that decreases specific energy and capacity. Disconnection describes the inability of the nanoparticle to exchange electrons with the current collector and/or ions with the electrolyte under externally applied voltage and current. Disconnection is usually explained by a combination of factors, including surface chemistry change, surface layer formation, particle cracking, particle movement, or a failure of contact between the particle and the conductive matrix[7,8]. However, understanding individual disconnection events is challenging as few techniques provide a direction measure of a particle's connectivity while also elucidating strain or ion concentration fields. As such, root causes of disconnection for specific materials are yet to be determined.

Electron microscopy[9,10] and X-ray microscopy[11–13] are useful tools for understanding degradation in battery nanoparticles, including cracking. However, both suffer from the inability to directly determine with a high degree of

accuracy whether or not the damaged particles are still connected. In addition, these techniques do not directly provide strain evolution and specialized sample environments can be required. Here we employ a technique known as coherent X-ray diffractive imaging (CXDI). CXDI in Bragg geometry is a powerful tool that relies on synchrotron produced coherent X-rays and their diffraction from crystalline samples[14–19]. The 3D electron density and atomic displacement fields are retrievable from coherent diffraction patterns with the use of phase retrieval algorithms[20,21]. Strain fields are the derivatives of the 3D displacement field components. Due to the high penetrating power of 9 keV X-rays, strain field information under *in-situ* conditions in real devices can be obtained, ensuring insight into real life processes[13,22,23]. 3D strain information is incredibly useful as a local Li concentration probe, in understanding structural dynamics during charge transfer, and in understanding defects and elastic material properties[14].

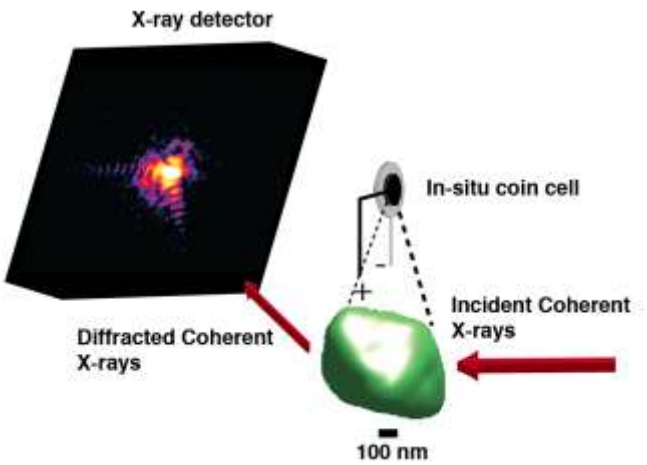

Fig. 1. Schematic of the experimental setup. Coherent X-rays are incident on an in-situ coin cell containing the cathode nanoparticle (green isosurface). Diffracted coherent X-rays are collected on a charge coupled device (CCD) detector downstream.

In Bragg geometry, the sensitivity of the monochromator (~10^{-4}) sets the measurement uncertainty in the lattice constant, orientation, and strain of the single particle[24]. In LNMO, the lattice constant varies proportionally with the lithium content, known as solid solution, from 3.5 V (fully discharged) to approximately 4.7 V. Thus measuring the lattice constant during solid solution provides a direct measure as to the particle's connectivity.

Experimental

Sample synthesis

$LiNi_{0.5}Mn_{1.5}O_{4-\delta}$ disordered spinel was synthesized using the sol gel method[17,25]. X-ray diffraction data (Supplementary Figure 1) and charge/discharge curves (Supplementary Figure 2) are in good agreement with the literature[26] and confirm both the Fd-3m unit cell structure and expected electrochemical performance. The electrochemical cell consisted of LNMO cathode and lithium metal anode. The electrolyte was a 1M solution of lithium hexafluorophosphate in a 1:1 volume mixture of ethylene carbonate and dimethyl carbonate.

Coherent diffraction experiment

A double crystal monochromator was used to select E=8.919 keV X-rays with 1 eV bandwidth and longitudinal coherence length of 0.7 μm. A set of Kirkpatrick Baez mirrors was used to focus the beam to 1 μm^2. The rocking curve around the (111) Bragg peak was collected by recording coherent diffraction patterns with a charge coupled device camera around $2\theta = 18°$ ($\Delta\theta = \pm 0.2°$). The particle was imaged after an equilibration procedure consisting of a 30-minute holding period at constant voltage followed by 30-minute relaxation to open circuit voltage. After this equilibration procedure, the lattice constant does not change. Three measurements were performed at each charge state and averaged together.

Phase retrieval

The phase retrieval code is adapted from published work[20,21] and augmented to include GPU capability. 90 iterations of the difference map algorithm[27] followed by ten iterations of the error reduction algorithm[28,29] were used and the algorithm converged after a total of 3150 iterations. The shrinkwrap algorithm[30] was used to update the support every five iterations. The data set for each reconstruction is formed by averaging at least 3 independent coherent diffraction measurements taken in succession at the same charge state. At least 10 reconstructions beginning from random phase starts were averaged for the final reconstruction. The final resolution of 40 nm was computed via the phase retrieval transfer function[31] (Supplementary Figure 3).

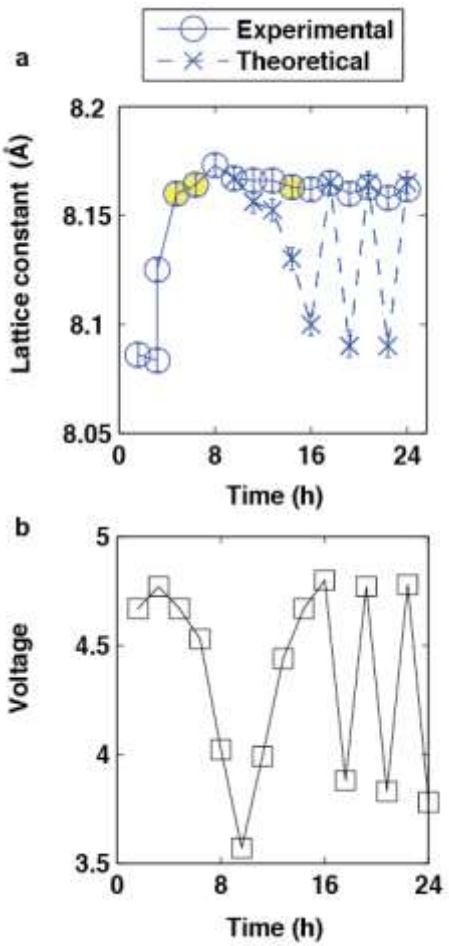

Fig. 2. Lattice constant evolution during charging and discharging. In Fig. 2a, the measured lattice evolution is shown in blue circles while the evolution for a connected particle during discharge is shown in dashed X. Note the lattice responds very weakly after 10 hours. Yellow highlighted points correspond to the states shown in Figure 3. Fig. 2b shows the open circuit voltage at which the measurements were taken.

Results and discussion

Figure 1 shows schematically the experimental setup. Coherent X-rays from the synchrotron are incident on an *in-situ* coin cell containing the battery cathode. The coin cell casting had a 5 mm opening, which was sealed with kapton film on both sides, to transmit X-rays. The windows do not significantly affect the electrochemical performance or the capacity retention as demonstrated by the electrochemical performance in the in-situ coin cell during X-ray exposure[19]. The cathode is approximately 80 microns thick and contains randomly orientated particles as shown by the electron microscopy image, Supplementary Figure 4. This construction yields well-separated reciprocal space lattice peaks corresponding to individual particles. The particle imaged in this work is octahedral in shape and approximately 600 nm across.

Figure 2a shows the average lattice constant of the single particle in blue circles during charging and discharging. The single particle lattice constant is determined by the location of the Bragg peak maximum according to Bragg's law. During discharge (Fig. 2b), the lattice increased as lithium is inserted, as expected[14,19]. Once fully discharged, the battery is charged and the lattice constant is expected to decrease as lithium is taken out of the particle. However, the lattice constant deviates from connected particle behaviour (dashed X values) and only slightly decreases during the charge cycle. The lattice constant changes very little during subsequent cycling between 3.5 V and 5 V after 16 hours. We thus conclude that one or both of the particle's conduction pathways are significantly changed after the 8-hour mark. We note that the battery loses some capacity during each cycle but continues to charge and discharge as expected indicating that most particles are still connected (see Supplementary Figure 6). To clarify, this is a different particle from previous work[14].

In a functional electrode, both electron and ion conductive pathways function such that charge rates such as C/2 (30 minutes for full charge) are possible. Ions conduct through the electrolyte while electrons travel through the conductive matrix, carbon black in this specific case, surrounding the cathode particles. Disconnection of one or both of these pathways can happen in several ways. One hypothesis is that the particle lost physical and/or electronic contact with the conductive matrix. The particle did not move more than 400 nm during this measurement due to the 1-micron beam size and 600 nm particle size. The particle could move a fraction of 400 nm, which would be sufficient for disconnection, but it would have to do so while maintaining its exact orientation because the Bragg reflection was continuously monitored without changing the sample position. The Bragg condition is sensitive to a rotation as small as 10^{-5} radians. Another hypothesis is that the conductive matrix surrounding the particle failed to accommodate the volume changes during cycling and the particle shrunk away losing contact. However, since the disconnection happens after discharge, in which the particle expands, this seems unlikely. In addition, the total volume change is only on the order of 1%. The particle could crack during the phase transformation, but this would most likely affect the orientation of a portion, or all, of the particle and result in a loss of intensity in the Bragg reflection, sensitive to a rotation as small as 10^{-5} radians, which we do not observe. A final hypothesis is that X-ray exposure contributed to the disconnection. However, we successfully imaged multiple particles throughout multiple charge/discharge cycles in three dimensions using the same X-ray dose without observing disconnection[14,32]. A change in surface chemistry resulting in larger ion impedance could also explain the observed behaviour.

The high operating voltage of this cathode makes it particularly susceptible to electrolyte decomposition. Unlike the layer formed at the anode, the so-called solid electrolyte interphase (SEI) layer[33–35], little is known about the analogous cathode layer[36]. This cathode layer, which could take 1-2 charge-discharge cycles to form, can effectively destroy the ion conduction pathway if the surface species formed are poor ion-conductors and thus limit ion diffusion[36]. Upon closer inspection of Fig. 2a, the lattice constant does change very slightly in the expected direction after the 8-hour mark. This implies that the particle can still respond but the timescale for ion transport is orders of magnitude slower than before, which is consistent with the formation of a surface layer. We estimate the capacity loss from the first to third cycle at approximately 1.5% (see Supplementary Figures 5-6). Assuming all capacity loss is due to disconnection of active material this corresponds to the disconnection of $1.5\text{x}10^7$ particles. $9.85\text{x}10^8$ particles are still connected.

We further investigated the cause of disconnection by utilizing the full three-dimensional displacement field along [111], $u_{111}(x,y,z)$, to compute the compressive/tensile strain field in this direction, $\partial_{111}u_{111}(x,y,z)$. We computed the strain with respect to the average lattice constant of the particle at the particular charge state given by Fig. 2a. Figure 3 shows 6 contour slices of the 3D compressive/tensile strain map at locations indicated by the particle rendering in Fig. 3a. The three charge states shown correspond to the yellow highlighted points in Fig. 2a. At t=6h (Fig. 3b.), large strain exists in both the core and the shell towards the bottom of the particle. This state is in the solid solution regime, so the compressive/tensile strain can be thought of as lithium poor and lithium rich regions, respectively. We thus can see significant lithium inhomogeneity in the bottom 3 contour slices of Fig. 3b. After the disconnection (Fig. 3c-d), a large region of tensile strain still exists in the particle boundary. This could be due to lithium trapped in a cathode electrolyte layer of approximately 50 nm. Figures 3c-d show that the strain map changes only slightly after t = 7 h, which is consistent with a disconnection event and very slow lattice variation as seen in Fig. 2a. The correlation between lattice constant change and strain field evolution shows that strain evolution is concomitant with lithium concentration changes. The strain field is not significantly governed by interactions with the environment (including neighbouring particles or the electrode) that continue to charge and discharge as normal.

Lithium rearrangement within the particle, which will not change the average lattice constant, on the timescale of the measurement does not occur after 7 hours since the strain field is unchanged. This is consistent with phase field models[37,38] that show concentration fields are determined by a competition between entropy, enthalpy, and coherency strain. Although the equilibration procedure of a 30-minute hold at constant voltage, followed by a 30-minute relaxation period to open circuit voltage occurs at each point, the particle's strain field is essentially unchanged. Lack of detectable changes in the strain

field, and by extension ion distribution, within the particle over 10 hours indicate the particle can be considered to be in quasi-equilibrium at all times.

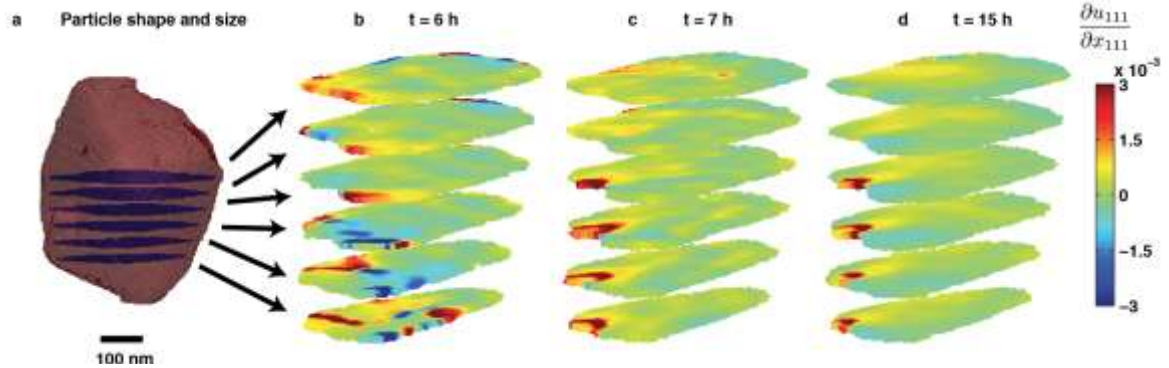

Fig. 3. 3D Strain evolution throughout the particle during the disconnection event. Compressive/tensile strain maps before and after the disconnection event are shown for 6 cross-sections located throughout the particle as shown in Fig. 2a. The red isosurface shows the particle shape while the blue slices show the 3D spatial location of the associated cross-section connected by black arrows. In Fig. 2b, significant strain inhomogeneity exists in both the core and the shell of the particle. In Fig. 2c-d, strain inhomogeneity is largely dissipated except in a surface layer.

We quantitatively investigate the disconnection event by evaluating the strain field energy. The strain field energy is the sum of the product of the stress and the strain integrated over the particle[39]. Under the assumptions of cubic symmetry and isotropic shear-free conditions in the unit cell, the strain field energy can be simplified to

$$E_s = \frac{2G + 3I}{2} \int \left(\frac{\partial u_{111}}{\partial x_{111}}\right)^2 dV$$

where G and I are the Lame constants for the material, estimated using molecular dynamics simulations of $LiMn_2O_4$ spinel[40], and the volume integral is over the particle. Figure 4 shows the evolution of strain field energy in the particle in response to externally applied voltage and current.

Initially, the strain energy is relatively low. However, during the structural phase transformation the energy increases more than ten fold, indicating a high amount of strain throughout the particle. This is consistent with structural phase transformations inducing large strains due to the maintenance of coherent interfaces between two phases of different lattice constants[2,37,41,42]. The energy then drops, with a slight modulation upwards before settling at the disconnected value. The fluctuations of the energy thereafter are due to measurement uncertainty, given by the width of the symbols, and the very slow variation in the lattice parameter as shown in Fig. 2a. The values we obtained are consistent with our previous results during discharge[14].

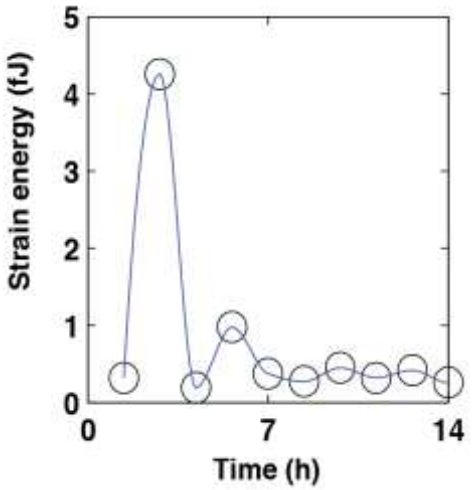

Fig. 4. Total strain energy (fJ) of the single nanoparticle in Fig. 3 during charging and discharging. The strain field energy peaks during the structural phase transformation before settling at the disconnected value. Uncertainty is given by the width of the symbols.

Conclusions

We revealed *in-situ* 3D strain evolution of a single cathode nanoparticle during a disconnection event. There are many possible disconnection causes for the particle we image, including particle movement, inelastic response of the conductive matrix, and significant particle cracking. The 3D strain map shows significant lithium inhomogeneity exists near the particle surface, which is consistent with the formation of a poorly conducting surface layer. Electrode engineering is clearly an essential component of improving battery life. Finally, the strain map remains static while the particle is effectively disconnected, indicating the particle is unable to rearrange lithium within the particle volume or exchange lithium with its neighbours. Thus, strain in this particle is primarily due to Li concentration and not interactions with the surrounding environment. CXDI is thus able to determine the connectivity of single battery nanoparticles, possible reasons for their disconnection, and the equilibrium or non-equilibrium state of single nanocrystals.

Acknowledgements

This work was supported by U.S. Department of Energy, Office of Science, Office of Basic Energy Sciences, under Contract DE-SC0001805. H.M.C. and Y.S.M. acknowledge the financial support by U.S. Department of Energy, Offi ce of Basic Energy Sciences, under Award Number DE-SC0002357. O.G.S. and Y.S.M. are grateful to the UCSD Chancellor's Interdisciplinary Collaborators Award that made this collaboration possible. Use of the Advanced Photon Source, an Office of Science User Facility operated for the U.S. Department of Energy (DOE) Office of Science by Argonne National Laboratory, was supported by the U.S. D.O.E. under Contract No. DE-AC02-06CH11357. A.U. thanks the staff at Argonne National Laboratory and the Advanced Photon Source for their support. J.N.C gratefully acknowledges financial support from the Volkswagen Foundation.

References

Electronic Supplementary Information (ESI) available: [details of any supplementary information available should be included here]. See DOI: 10.1039/b000000x/

1. M. Armand and J.-M. Tarascon, *Nature*, 2008, **451**, 652–657.
2. A. S. Aricò, P. Bruce, B. Scrosati, J.-M. Tarascon, and W. van Schalkwijk, *Nat. Mater.*, 2005, **4**, 366–77.
3. H. Deng, I. Belharouak, R. E. Cook, H. Wu, Y.-K. Sun, and K. Amine, *J. Electrochem. Soc.*, 2010, **157**, A447.
4. Y.-K. Sun, C. S. Yoon, C. K. Kim, S. G. Youn, Y.-S. Lee, M. Yoshio, and I.-H. Oh, *J. Mater. Chem.*, 2001, **11**, 2519–2522.
5. J. Christensen and J. Newman, *J. Solid State Electrochem.*, 2006, **10**, 293–319.
6. J. Vetter, P. Novák, M. R. Wagner, C. Veit, K.-C. Möller, J. O. Besenhard, M. Winter, M. Wohlfahrt-Mehrens, C. Vogler, and a. Hammouche, *J. Power Sources*, 2005, **147**, 269–281.
7. D. Chen, Thesis. Karlsruher Institut fur Technologie, 2012.
8. J. S. Peña, I. Sandu, O. Joubert, F. S. Pascual, C. O. Areán, and T. Brousse, *Electrochem. Solid-State Lett.*, 2004, **7**, A278.
9. H. Wang, Y. Jang, and B. Huang, *J. Electrochem. Soc.*, 1999, **146**, 473–480.
10. S. Meister, S. Kim, J. J. Cha, H.-S. P. Wong, and Y. Cui, *ACS Nano*, 2011, **5**, 2742–8.
11. M. Ebner, F. Marone, M. Stampanoni, and V. Wood, *Science*, 2013, **342**, 716–20.
12. Y. Li, F. El Gabaly, T. R. Ferguson, R. B. Smith, N. C. Bartelt, J. D. Sugar, K. R. Fenton, D. A. Cogswell, A. L. D. Kilcoyne, T. Tyliszczak, M. Z. Bazant, and W. C. Chueh, *Nat. Mater.*, 2014, 1–8.
13. J. N. Weker, N. Liu, S. Misra, J. C. Andrews, Y. Cui, and M. F. Toney, *Energy Environ. Sci.*, 2014, **7**, 2771.
14. A. Ulvestad, A. Singer, H.-M. Cho, J. N. Clark, R. Harder, J. Maser, Y. S. Meng, and O. G. Shpyrko, *Nano Lett.*, 2014.
15. I. Robinson and R. Harder, *Nat. Mater.*, 2009, **8**, 291–8.
16. J. N. Clark, X. Huang, R. Harder, and I. K. Robinson, *Nat. Commun.*, 2012, **3**, 993.
17. A. Ulvestad, H. M. Cho, R. Harder, J. W. Kim, S. H. Dietze, E. Fohtung, Y. S. Meng, and O. G. Shpyrko, *Appl. Phys. Lett.*, 2014, **073108**, 2–6.
18. J. N. Clark, L. Beitra, G. Xiong, a Higginbotham, D. M. Fritz, H. T. Lemke, D. Zhu, M. Chollet, G. J. Williams, M. Messerschmidt, B. Abbey, R. J. Harder, a M. Korsunsky, J. S. Wark, and I. K. Robinson, *Science*, 2013, **341**, 56–9.
19. A. Singer, A. P. Ulvestad, H.-M. Cho, J. W. Kim, J. Maser, R. Harder, Y. S. Meng, and O. G. Shpyrko, *Nano Lett.*, 2014, **14**, 5295–5300.
20. I. Robinson, *J. Phys. Soc. Japan*, 2012, **82**, 21012.
21. R. Harder and I. K. Robinson, *Jom*, 2013, **65**, 1202–1207.
22. C.-M. Wang, X. Li, Z. Wang, W. Xu, J. Liu, F. Gao, L. Kovarik, J.-G. Zhang, J. Howe, D. J. Burton, Z. Liu, X. Xiao, S. Thevuthasan, and D. R. Baer, *Nano Lett.*, 2012, **12**, 1624–32.
23. M. E. Holtz, Y. Yu, D. Gunceler, J. Gao, R. Sundararaman, K. A. Schwarz, T. A. Arias, H. D. Abruña, and D. A. Muller, *Nano Lett.*, 2014, **14**, 1453–9.
24. M. Watari, R. a McKendry, M. Vögtli, G. Aeppli, Y.-A. Soh, X. Shi, G. Xiong, X. Huang, R. Harder, and I. K. Robinson, *Nat. Mater.*, 2011, **10**, 862–6.
25. H.-M. Cho and Y. S. Meng, *J. Electrochem. Soc.*, 2013, **160**, A1482–A1488.
26. J.-H. Kim, C. S. Yoon, S.-T. Myung, J. Prakash, and Y.-K. Sun, *Electrochem. Solid-State Lett.*, 2004, **7**, A216.
27. V. Elser, I. Rankenburg, and P. Thibault, *Proc. Natl. Acad. Sci. U. S. A.*, 2007, **104**, 418–423.
28. J. R. Fienup and A. M. Kowalczyk, *J. Opt. Soc. Am. A*, 1990, **7**, 450.
29. J. R. Fienup, *Appl. Opt.*, 1982, **21**, 2758–69.
30. S. Marchesini, H. He, and H. Chapman, *Phys. Rev. B*, 2003, 1–5.
31. A. Tripathi, J. Mohanty, S. H. Dietze, O. G. Shpyrko, E. Shipton, E. E. Fullerton, S. S. Kim, and I. McNulty, *Proc. Natl. Acad. Sci. U. S. A.*, 2011, **108**, 13393–8.
32. A. Ulvestad, A. Singer, J. N. Clark, H. M. Cho, J. W. Kim, R. Harder, J. Maser, and Y. S. Meng, *Sci. (under Rev.*

33. E. Peled, *J. Electrochem. Soc.*, 1979, 2047–2051.

34. P. Arora, R. White, and M. Doyle, *J. Electrochem. Soc.*, 1998, **145**, 3647–3667.

35. Z. Zeng, W.-I. Liang, H.-G. Liao, H. L. Xin, Y.-H. Chu, and H. Zheng, *Nano Lett.*, 2014, **14**, 1745–50.

36. H. Duncan, Y. Abu-Lebdeh, and I. J. Davidson, *J. Electrochem. Soc.*, 2010, **157**, A528.

37. D. A. Cogswell and M. Z. Bazant, *ACS Nano*, 2012, **6**, 2215–25.

38. P. Bai, D. A. Cogswell, and M. Z. Bazant, *Nano Lett.*, 2011, **11**, 4890–6.

39. J. W. Cahn, *J. Chem. Phys.*, 1959, **30**, 1121.

40. S. Lee, J. Park, A. M. Sastry, and W. Lu, *J. Electrochem. Soc.*, 2013, **160**, A968–A972.

41. Y.-K. Sun, Z. Chen, H.-J. Noh, D.-J. Lee, H.-G. Jung, Y. Ren, S. Wang, C. S. Yoon, S.-T. Myung, and K. Amine, *Nat. Mater.*, 2012, **11**, 942–7.

42. A. Van der Ven, K. Garikipati, S. Kim, and M. Wagemaker, *J. Electrochem. Soc.*, 2009, **156**, A949.

